AGU PUBLICATIONS

JGR

Journal of Geophysical Research: Solid Earth

RESEARCH ARTICLE

10.1002/2014JB011519

P. A. Ashwell and J. E., Kendrick contributed equally.

Key Points:
- Porous lavas compact by pore wall failure and viscous flow
- Compaction causes strain hardening: viscosity increases, strain rate decreases
- The presence of crystals hinders compaction and reduces maximum crack length

Supporting Information:
- Text S1
- Movie S1
- Movie S2
- Movie S3
- Movie S4
- Movie S5
- Movie S6

Correspondence to:
J. E. Kendrick,
jackie.kendrick@liverpool.ac.uk

Citation:
Ashwell, P. A., J. E. Kendrick, Y. Lavallée, B. M. Kennedy, K.-U. Hess, F. W. von Aulock, F. B. Wadsworth, J. Vasseur, and D. B. Dingwell (2015), Permeability of compacting porous lavas, *J. Geophys. Res. Solid Earth*, *120*, 1605–1622 doi:10.1002/2014JB011519.

Received 11 AUG 2014
Accepted 1 FEB 2015
Accepted article online 5 MAR 2015
Published online 31 MAR 2015

Permeability of compacting porous lavas

P. A. Ashwell[1], J. E. Kendrick[2], Y. Lavallée[2], B. M. Kennedy[1], K.-U. Hess[3], F. W. von Aulock[2], F. B. Wadsworth[3], J. Vasseur[3], and D. B. Dingwell[3]

[1]Geological Sciences, University of Canterbury, Christchurch, New Zealand, [2]Earth, Ocean and Ecological Sciences, University of Liverpool, Liverpool, UK, [3]Earth and Environmental Sciences, Ludwig Maximilian University of Munich, Munich, Germany

Abstract The highly transient nature of outgassing commonly observed at volcanoes is in part controlled by the permeability of lava domes and shallow conduits. Lava domes generally consist of a porous outer carapace surrounding a denser lava core with internal shear zones of variable porosity. Here we examine densification using uniaxial compression experiments on variably crystalline and porous rhyolitic dome lavas from the Taupo Volcanic Zone. Experiments were conducted at 900°C and an applied stress of 3 MPa to 60% strain, while monitoring acoustic emissions to track cracking. The evolution of the porous network was assessed via X-ray computed tomography, He-pycnometry, and relative gas permeability. High starting connected porosities led to low apparent viscosities and high strain rates, initially accompanied by abundant acoustic emissions. As compaction ensued, the lavas evolved; apparent viscosity increased and strain rate decreased due to strain hardening of the suspensions. Permeability fluctuations resulted from the interplay between viscous flow and brittle failure. Where phenocrysts were abundant, cracks had limited spatial extent, and pore closure decreased axial and radial permeability proportionally, maintaining the initial anisotropy. In crystal-poor lavas, axial cracks had a more profound effect, and permeability anisotropy switched to favor axial flow. Irrespective of porosity, both crystalline samples compacted to a threshold minimum porosity of 17–19%, whereas the crystal-poor sample did not achieve its compaction limit. This indicates that unconfined loading of porous dome lavas does not necessarily form an impermeable plug and may be hindered, in part by the presence of crystals.

1. Introduction

Dome-building eruptions involve a complex competition between crystallization [*Cashman et al.*, 2000; *Sparks et al.*, 2000; *Cashman et al.*, 2008; *Humphreys et al.*, 2008], bubble nucleation, growth, coalescence and outgassing [*Kennedy et al.*, 2010; *von Aulock*, 2013], bulk magma deformation [*Smith et al.*, 2001; *Lavallée et al.*, 2007; *Cordonnier et al.*, 2009; *Okumura et al.*, 2009; *Caricchi et al.*, 2011; *Avard and Whittington*, 2012], and crack propagation and healing [*Tuffen et al.*, 2003; *Cabrera et al.*, 2011; *Castro et al.*, 2012a; *Kolzenburg et al.*, 2012]. These processes create and destroy the permeable degassing pathways that ultimately dictate the explosivity and/or stability of the lava dome [*Klug and Cashman*, 1996; *Smith et al.*, 2001; *Rust and Cashman*, 2004; *Mueller et al.*, 2005; *Takeuchi et al.*, 2005; *Edmonds and Herd*, 2007; *Hale and Wadge*, 2008; *Mueller et al.*, 2008; *Nakamura et al.*, 2008; *Takeuchi et al.*, 2008; *Wright et al.*, 2009; *Kendrick et al.*, 2013]. Lava domes generally result from the extrusion of highly viscous magmas [*Fink et al.*, 1992; *Matthews et al.*, 1997; *Sparks*, 1997; *Yoshimura and Nakamura*, 2008; *Lavallée et al.*, 2013], with wide ranging composition (andesitic to rhyolitic), porosity, and crystallinity (~0–100%). The growth of lava domes can be either endogenous, occurring through inflation of the dome carapace by magma injection, or exogenous, occurring through a series of extrusions of individual lava lobes and spines [*Nakada et al.*, 1999]. Structural analysis of endogenous lava domes has revealed that they commonly have a variably porous and brecciated carapace surrounding a denser, coherent, often foliated interior [*Fink et al.*, 1992; *Wadge et al.*, 2009]. In contrast, internal structures in exogenous lava domes are largely derived from magma ascent in the conduit [e.g., *Hale and Wadge*, 2008]. Strain localization in exogenous lava domes is induced by competing deformation mechanisms partitioned between the melt, crystal, and gas phases [*Caricchi et al.*, 2007; *Wright and Weinberg*, 2009; *Holland et al.*, 2011; *Lavallée et al.*, 2012; *Kendrick et al.*, 2013; *Lavallée et al.*, 2013] and leads to heterogeneous distribution of porosity [*Nakada et al.*, 1999; *Watts et al.*, 2002; *Vallance et al.*, 2008; *Gaunt et al.*, 2014].

The nature of the permeable network inside a dome controls the efficiency of outgassing, and thus the internal pore network pressure. If the deformation rate induced by the bubble growth [*Sparks*, 1978] exceeds

the structural relaxation timescale of the melt (i.e., the timescale that dictates the structural transition about which melt behaves as a relaxed liquid or an unrelaxed glass [see *Dingwell and Webb*, 1989]), fragmentation of the magma will ensue [*Mueller et al*., 2008]. Importantly, the amount and distribution of gas overpressure inside the dome will dictate whether the dome rock will either fracture to form a permeable network or be completely excavated by an explosive eruption [*Matthews et al*., 1997; *Herd et al*., 2005; *Mueller et al*., 2005; *Loughlin et al*., 2010; *Okumura and Sasaki*, 2014]. Thus, it is crucial to consider the permeability of dome structures on multiple scales and its impact on the broader volcanic system.

Macroscopically, large damage zones (caused by recurring gas and ash explosions or sustained shear) or facies boundaries (e.g., fault gouge, breccia, or shear zones) in exogenous lava domes form extensive structures that feed and channel gas and ash explosions and bleed large regions of the dome by inducing relatively steep gas pressure gradients [*Johnson et al*., 2008; *Sahetapy-Engel and Harris*, 2008; *Collinson and Neuberg*, 2012; *Schipper et al*., 2013; *Kendrick et al*., 2013]. The permeability of these structures is anisotropic; laboratory-scale measurements have indicated that vertical movement of gas in shear zones is far more efficient than lateral [*Kendrick et al*., 2014; *Gaunt et al*., 2014]. Microscopically, permeability in lava domes is controlled by the size and shape, as well as the proportions and interconnectivity of pores and microcracks [e.g., *Mueller et al*., 2005; *Wright et al*., 2009; *Bouvet de Maisonneuve et al*., 2009; *Yokoyama and Takeuchi*, 2009; *Nara et al*., 2011; *von Aulock et al*., 2013; *Kendrick et al*., 2013; *Okumura and Sasaki*, 2014] and, specifically, their ability to nucleate [e.g., *Sparks*, 1978; *Proussevitch and Sahagian,* 1996], grow [e.g., *Lovejoy et al*., 2004; *Castro et al*., 2012b; *Cashman and Sparks*, 2013], coalesce [e.g., *Klug and Cashman*, 1996; *Takeuchi et al*., 2008; *Okumura et al*., 2009; *Laumonier et al*., 2011], and collapse or heal [e.g., *Tuffen et al*., 2003; *Cabrera et al*., 2011; *Castro et al*., 2012a; *Vasseur et al*., 2013; *Wadsworth et al*., 2014]. Across all scales, shear zones, cracks and fractures, cavities, and flow bands can locally accentuate anisotropy and alter the permeable network [*Smith et al*., 2001; *Hale and Wadge*, 2008; *Okumura et al*., 2009; *Laumonier et al*., 2011; *Avard and Whittington*, 2012; *Castro et al*., 2012a; *Lavallée et al*., 2013]. Although the complex interplay between pores and cracks at both microscopic and macroscopic scales is crucial to understanding lava dome eruptions, the permeability relationships remain elusive.

2. Lava Dome Architecture

Dissected outcrops allowing access to the interior portions of the internal structures at Ngongotaha dome and Ruawahia dome, in the Taupo Volcanic Zone, New Zealand, were examined and were found to exhibit intricate and mechanically informative internal kinematic structures. These structures provide a conceptual framework for the samples used in this study.

Ngongotaha dome is a ~4 km diameter rhyolitic (74–75 wt % SiO_2) lava dome consisting of six individual flow lobes, each between 200 and 400 m thick, erupted circa 200 ka, following the Mamaku eruptions that produced Rotorua caldera [*Ashwell et al*., 2013]. The pumiceous carapace of Ngongotaha is 20 to 40 m thick and has low crystallinity (phenocrysts equal 3–5 vol % of the solid fraction, with no microlites present), elongate pores (total porosity typically ranging from 50 to 58%), and minor amounts of spherulitic crystallization (thought to be posteruptive) in comparison to the denser dome interior. In contrast, the center of a lava lobe at Ngongotaha dome is exposed by quarrying and contains low-porosity ($<$10%) devitrified obsidian, with near-horizontal flow banding indicating a lateral flow direction from a central, elongate vent [*Ashwell et al*., 2013]. Directly above this vent are vertically emplaced, poorly flow banded obsidian sheets bounded by breccia zones, suggesting a change to the extrusion of vertical sheets of obsidian late in the eruption [*Ashwell*, 2014]. No change in phenocryst content is noted throughout the extrusion of this lobe.

Ruawahia dome is a ~1.5 km diameter, 150 to 250 m thick rhyolitic (76–77 wt % SiO_2) lava dome formed during the A.D. 1314 Kaharoa eruption at Tarawera dome complex and Okataina caldera complex [*Cole*, 1970; *Nairn et al*., 2001, 2004]. At an average 65 vol % of the solid fraction, the dome has higher phenocryst content (it also contains no microlites) than Ngongotaha. The core of Ruawahia dome is exposed by the A.D. 1886 eruptive fissure [*Cole*, 1970] has a moderate connected porosity (22–26%), and is devitrified and spherulite rich with flow units containing deformed, elongate vesicles. The carapace is 10 to 25 m thick and is weakly flow banded, with little to no devitrification, and has a higher porosity (typically 25–35%) compared to the dome interior. Locally, the carapace is much more porous (up to 55%) with areas that contain well-rounded pores, indicative of in situ bubble growth (little to no postvesiculation strain). Overall, the dome consists of several

individual lobes that vary in size from 200 m diameter lava domes confined in an earlier pyroclastic cone, to 1 km long, ~250 m wide lavas on the flanks of the cone [*Ashwell*, 2014]. These lobes can be differentiated by flow band orientations and are separated by narrow breccia zones [*Ashwell*, 2014]. The blocks in block-and-ash flow deposits generated during dome extrusion [*Nairn et al.*, 2001] show a larger variation in vesicularity, ranging from dense obsidian (5–10% porosity) to inflated breadcrust bombs (<64% porosity) and generally contain fewer spherulites and more pristine glass than the interior of the dome.

3. Samples and Methods

Three natural samples with different crystallinity and porosity were selected to assess the evolution in permeability of dome lavas when subjected to compression.

1. NP (Ngongotaha Pumiceous). A finely vesicular (49–57% total porosity), crystal-poor (~5% of the solid fraction) pumice from the breccia of the dome carapace at Ngongotaha (rapid quenching at extrusion preserved the pores), with dominantly small, elongate pores (~30 μm to 500 μm) and some areas of large, irregularly shaped pores (from 0.5 mm to 5 mm) leading to a strong permeability anisotropy.
2. TP (Tarawera Pumiceous). A vesicular (44–52% total porosity), crystal-rich (60–65% of the solid fraction) lava with a large range of pore sizes (50 μm to 2 mm), from a block-and-ash flow deposit generated from Ruawahia dome (assumed to represent the eruptive porosity due to the rapid, explosive expulsion of the lava and inferred from its lack of spherical, nonflow-deformed bubbles that represent in situ vesiculation).
3. TD (Tarawera Dense). A moderately vesicular (23–26% total porosity), crystal-rich (65–70% of the solid fraction) dome rock with and highly elongate pores (~150 μm) and a few small pores (~30 μm) from the same block-and-ash flow that generated TP.

These samples were chosen because they have similar glass chemistry (Table 1); therefore, a comparison between NP and TP explores the effect of crystallinity, while comparison of TP and TD provides insights on the effects of porosity.

3.1. Compaction

The rocks were cored into cylindrical samples (25 mm diameter and 50 mm length) perpendicular to pore elongation. One core of each sample was then heated and cooled at a rate of 2°C/min to a target sample temperature of 900°C (monitored by a thermocouple inserted into a hole drilled in the sample) in a box furnace to monitor the effects of temperature alone. The porosity before and after this process was measured to be <2% different, and so the effect is considered minimal compared to the deformation-induced changes. For the experiments, each core was individually mounted into a uniaxial deformation press at Ludwig Maximilian University of Munich [see *Hess et al.*, 2007] and heated to 900°C (temperature monitored by a thermocouple in contact with the sample) at 2°C/min to minimize thermal stressing effects. The sample was allowed to dwell at 900°C for >1 h This experimental dwell time is sufficient for water content to equilibrate with atmospheric pressure for porous rhyolitic magma at 900°C with water content <1 wt % (dominantly molecular water) [*Kennedy et al.*, 2010]. The loss of water was confirmed by loss on ignition (LOI) measurements, in which the sample was heated to 1000°C (Table 1). Once thermally equilibrated load was applied and held at a constant compressive stress of 3 MPa (equivalent to an overburden of approximately 150 m, i.e., at the base of the lava domes studied), which was maintained until a given strain increment (10, 20, 30, 40, 50, or 60%) was achieved (Figure 1). Acoustic emissions were monitored by sensors in the top and bottom anvils (while the piston was in contact with the sample) to monitor cracking. Once the cores had deformed, the load was removed and the cores were cooled at 2°C/min.

3.2. Viscosity

During compaction the load and axial displacement (cf. strain) were recorded and the transient apparent viscosity of the suspension was calculated via a modification of the *Gent* [1960] equation developed for a parallel-plate compression viscometer:

$$\eta_a = \frac{2\pi F h^5}{3V\mathrm{d}h/\mathrm{d}t\left(2\pi h^3 + V\right)} \quad (1)$$

where h is the time-dependent sample height (m), F is force applied (N), and V is the initial sample volume (m^3). Apparent viscosity (η_a) is therefore a measured relationship between stress and strain rate at a defined stress. To

Table 1. Interstitial Glass Chemistry in Weight Percent Oxides by Microprobe Analysis in a CAMECA SX100 Using a Defocused 10 μm Beam, With a 15 kV Accelerating Voltage and 5 nA Current[a]

	Na_2O	Al_2O_3	K_2O	CaO	TiO_2	FeO	MnO	MgO	P_2O_5	SiO_2	Cl	Total	H_2O LOI
NPR	4.03 ± 0.17	12.13 ± 0.20	3.20 ± 0.40	0.90 ± 0.05	0.16 ± 0.05	1.36 ± 0.09	0.06 ± 0.04	0.12 ± 0.02	0.00 ± 0.06	76.52 ± 1.49	0.18 ± 0.04	98.59	0.0
TPR	3.80 ± 0.13	12.07 ± 0.24	3.79 ± 0.19	0.58 ± 0.07	0.08 ± 0.04	0.84 ± 0.12	0.06 ± 0.06	0.06 ± 0.03	0.00 ± 0.05	78.47 ± 1.37	0.16 ± 0.06	99.91	0.1
TDR	3.78 ± 0.13	12.17 ± 0.26	3.91 ± 0.18	0.59 ± 0.06	0.08 ± 0.05	0.83 ± 0.07	0.06 ± 0.06	0.06 ± 0.02	0.00 ± 0.07	77.97 ± 1.78	0.15 ± 0.04	99.60	0.1

[a]The measurements below represent an average of 45 to 60 measurements per sample and ± indicates the variability of measurements, which is larger than the error on individual measurement. LOI (loss on ignition) is the mass loss by heating to 1000°C.

discriminate the rheological effects of phenocryst content and pore fraction from that of the minimally variable melt viscosities (resulting from slightly different glass compositions of experimental samples; Table 1), we consider the relative viscosity (η_r), which is the ratio of the measured apparent viscosity to that of the idealized interstitial melt viscosity (η_o):

$$\eta_r = \eta_a/\eta_o. \tag{2}$$

The melt viscosity (η_o) was calculated using the model of *Giordano et al*. [2008] with glass chemical composition (analyzed by microprobe, Table 1), a water content of 0 wt %, and the sample temperature (monitored by a thermocouple throughout the experiment) as input parameters. No water was present or lost during the experiment as water content was allowed to equilibrate during dwell time. The monitored temperature indicates that no measureable viscous heating took place due to the low applied load conditions and low resultant bulk strain rates [cf. *Hess et al*., 2008]. The modeled interstitial melt viscosity of the three samples, NP, TP, and TD, is comparable, and the effects of slight compositional differences are removed entirely in the relative viscosity calculation, which allows direct comparison of the effect pores and phenocrysts.

3.3. Tracking the Permeable Network

Fractures induced by the compaction were monitored via acoustic emission (AE) sensors. AEs (exceeding a threshold of 35 dB) were monitored at 5 MHz via two wideband acoustic sensors (optimized between 100 and 1000 kHz) preamplified by 20 dB. The porosity of each core, before and after deformation, was measured by He-pycnometry in an Accupyc 1330 from micrometrics (uncertainty for this measurement is associated with the sample dimensions and is considered to be $<4\%$ of the absolute value). For selected samples (0, 10, 50, and 60% strain), X-ray computed tomographic (micro-CT) imaging was utilized to reconstruct the 3-D structures of the permeable porous network. Tomographic reconstructions were achieved in two ways: at the Ludwig Maximilian University of Munich, the cores with 0 and 50% strain were imaged using a high power X-ray tube and a drx-250rt detector system with a voxel size of 14.78 μm and at the Australian synchrotron, the cores with 10 and 60% strain were imaged using the "Ruby" detector at a voxel size resolution of 6.1 μm.

Following these nondestructive, postdeformation analyses, the samples were recored into two smaller cylinders of 10 mm diameter, 8 to 25 mm in length, orientated parallel and perpendicular to the initial sample geometry to assess the axial versus radial permeability anisotropy of the deformed cores as compared to cores of the starting materials of the same size. Permeability measurements were performed with compressed air in a gas permeameter assembled at the University of Canterbury following the designs developed by *Takeuchi et al*. [2008]. The samples were jacketed in a rubber tube and set in resin before being sealed and clamped by a plug with gas inlet/outlet at each end. No confining pressure was applied to the sample during measurements. The permeability measurements were performed by setting a gas pressure gradient (ΔP) of -7 to -300 kPa across the sample (of length L and cross sectional area A), and the discharge rate (Q) was monitored; the permeability (K) was calculated using Darcy's law:

$$K = \frac{-Q\mu L}{A\Delta P} \tag{3}$$

where μ is the air viscosity (1.8×10^{-5} Pa s) at ambient conditions.

The lavas have naturally anisotropic permeability, and in the present study, we chose to deform cores along the axis with the lowest permeability (i.e., the radial permeability, K_r, was higher than the axial permeability, K_a, in the starting materials) as this is the dominant orientation of the in situ samples in the respective lava domes.

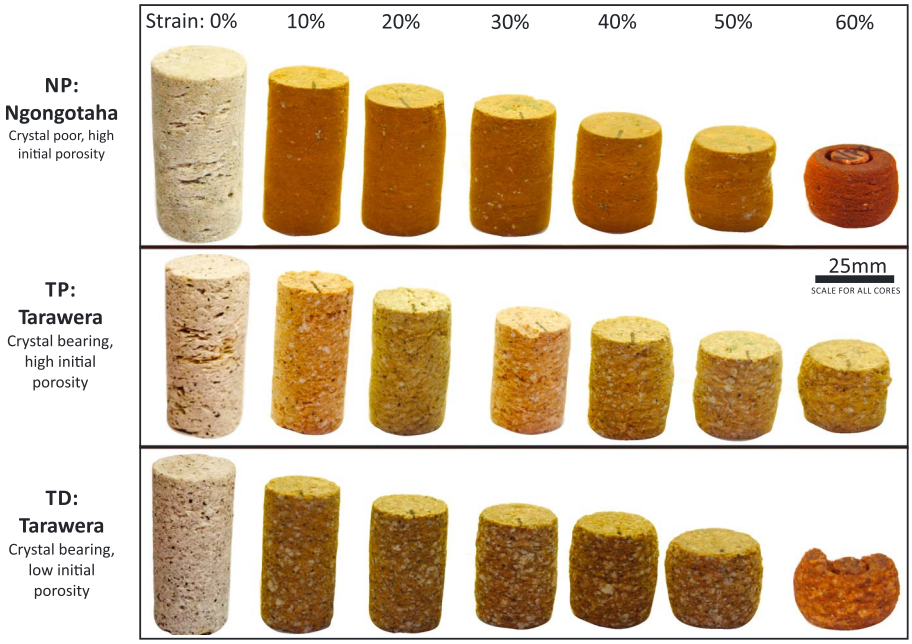

Figure 1. Photographs of cores at each axial strain increment showing lateral bulging, which is comparable in samples NP and TP, and most prominent in sample TD. (Samples NP and TD that were subjected to 60% strain have been recored for permeability before photograph.)

4. Results

4.1. Compaction Mechanics

Uniaxial compression induced a mechanical response distinct for all three samples. Compaction accommodated most of the deformation, with a minor amount of lateral bulging. Bulging initiated at lower strain in the dense lava, TD, than in the more porous lavas, NP and TP (Figure 1). We note that in the presence of crystals (TP versus NP) the compaction timescale to achieve the same strain increased (Figures 2a and 2b). Likewise, when the initial material is denser (TD versus TP) the time required to undergo the same strain also increased (Figures 2b and 2c). The constant stress initially produced a relatively high strain rate for all samples (Figure 2), which nonlinearly decreased with time (Figure 2d) and strain (Figure 3a). Deformation was accompanied by AE events generated by cracking (Figure 2). The majority of the acoustic events occurred during the initial portion of deformation (from 0 to 5% strain), when the strain rate was highest (Figures 3a and 3b) and viscosity lowest (Figures 3c and 3d). The strain rate of NP was the highest measured at the onset of deformation and followed a similar nonlinear decay as measured in TP at the same conditions and remained higher at the equivalent strain throughout (Figure 3a), as porosity was removed (Figures 4a and 4b). The strain rate was lower initially and decreased less for TD, such that the strain rate of TD and TP became equal at 50% strain (Figure 3a), coincident with achieving a minimum porosity threshold of 17–19% (Figures 4b–4d).

The evolution of microstructures during compaction translated to a nonlinear increase in the apparent viscosity of these suspensions with time and strain (Figure 3c). This evolution of magma viscosity during deformation is referred to as strain hardening, a rheological behavior which describes the increase in viscosity as the three-phase suspension reorganizes or phases are incrementally removed (e.g., outgassing of connected pores). The apparent viscosity of the crystal-poor NP sample was initially lower than in the crystal-rich TP and TD samples. For all samples, viscosity increased rapidly in the early portion of loading ($<$5% strain), most significantly for TD, viscosity then increased steadily until 50% strain, with TP and NP samples evolving similarly and the TD sample evolving more slowly, showing that the rate of strain hardening was similar to the porosity reduction rate of the samples during compaction (Figures 4a–4d). Throughout, it remained that the crystal-rich, lowest porosity TD was most viscous, and the lowest viscosity was in the crystal-poor, higher-porosity NP. For all samples, apparent viscosity increased by approximately 1 order of magnitude from 0 to 50% strain (Figure 3c).

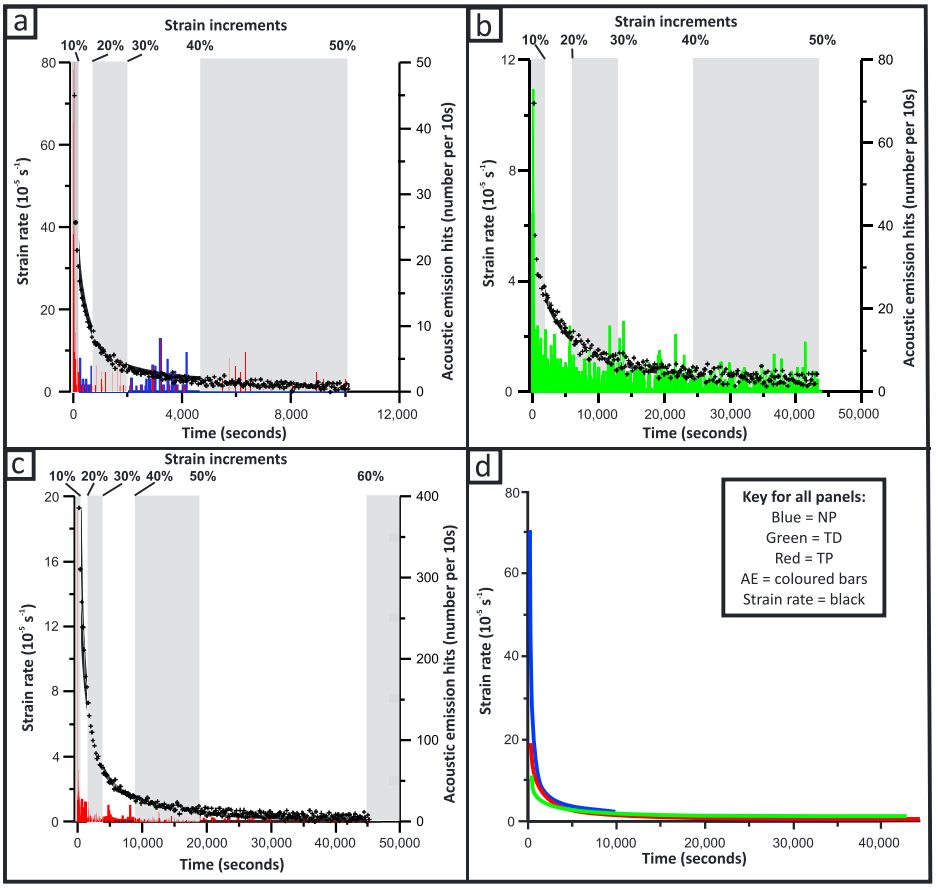

Figure 2. Strain rate and acoustic emission (AE) hits in 10 s bins during uniaxial compression at 900°C for (a) NP to 50% strain, (b) TD to 50% strain, (c) TP to 60% strain, and (d) a comparison of strain rates for the same experiments. Strain rate calculations are made over 10 displacement measurements in 0.1 s.

To eliminate the effect of interstitial melt composition on sample viscosity, and to directly compare pore and crystal content, we use the relative viscosity, which shows trends similar to those observed for the apparent viscosity (Figures 3c and 3d). This observation also highlights the different structural attributes of the samples, showing that the crystal-poor NP sample has a lower apparent viscosity than a Newtonian melt of that composition would have alone. The higher crystallinity of TP (as compared to NP) creates a higher apparent viscosity. Finally, the lower porosity of TD creates a higher relative viscosity (relative to TP).

4.2. Evolution of the Permeable Porous Network

The porosity and permeability evolution of the samples provides us with a physical basis for the mechanical response monitored during the experiments (Figure 4). Compaction resulted in a nonlinear, decelerating reduction in porosity over time (Figures 4a–4c), which manifests as an approximately linear porosity decrease with axial strain (Figure 4d). This decrease persisted until a threshold minimum porosity was achieved at 17–19% porosity, at 50 to 60% strain for crystal-rich TD and TP. For NP the porosity continued to decrease to at least 60% strain (where porosity was 14%) and could be expected to achieve an unknown lower porosity threshold at higher strain. This lower threshold is unlikely to be 0% porosity, as there is a limit to the amount of porosity that can be destroyed by compaction and surface tension alone [*Vasseur et al.*, 2013; *Wadsworth et al.*, 2014].

Due to inherent sample heterogeneity, measured permeability varied by up to 1 log unit along a single sample orientation. This is consistent with natural variation in porosities (and crack to pore ratios) of the cores used for these experiments (NP = 50–58%; TP = 44–52%; TD = 23–26%). The fabric inherent to each sample creates strongly anisotropic permeability; permeability parallel to pore elongation is 4 to 5 orders of

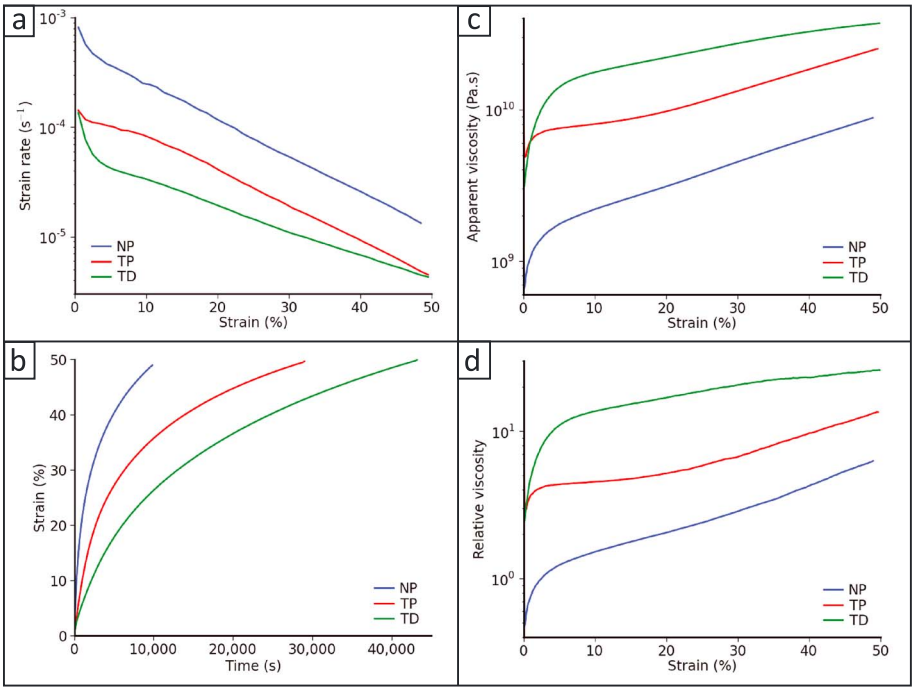

Figure 3. Evolution of lavas during compaction to 50% strain, including (a) strain rate decrease with increasing strain, (b) nonlinear increase in strain with time, (c) apparent viscosity increase due to strain hardening, and (d) relative viscosity increase with strain, which show that strain rate is lowest in TD and highest in NP and correspondingly, TD is highest viscosity and NP lowest. All values are calculated from 10 displacement measurements in 0.1 s to smooth the plots; uncertainty is under 0.1 log units.

magnitude higher than perpendicular to pore elongation for all samples (Figures 4e–4g). Pores were orientated perpendicular to the axis of compression. The permeability of the crystal-poor NP lava was more severely affected by compaction than the crystal-rich TP and TD lavas: We note a cross over in permeability anisotropy in the crystal-poor NP lava, where the axial permeability increases beyond the continuously decreasing radial permeability after ~20–30% strain, before 40% strain (Figure 4e). In the crystal-rich lavas, both the axial and radial permeability decrease during compaction and porosity loss until 40–50% strain (Figure 4h), but the magnitude of the anisotropy remains constant (Figures 4f and 4g). Increasing strain to 60% slightly increases permeability in TP and TD (Figure 4h), but again, anisotropy remains approximately constant (Figures 4f and 4g).

In all but one instance, porosity and permeability decrease simultaneously (Figure 5). In the crystal-poor NP sample, radial permeability decreases as porosity is reduced during strain; however, the axial permeability increases (Figure 5a), causing a reversal in the anisotropy of permeability. The axial permeability increases even as porosity decreases, indicating a shift in macroscopic structure of the crystal-poor NP sample. In samples TP and TD, the axial and radial permeability both decrease as porosity reduces due to compaction (Figures 5b and 5c), similar to the radial permeability of sample NP. The crystal-bearing TP and TD samples have similar (but slightly decreasing) permeability anisotropy throughout the compaction process, and although in TD permeability and porosity actually increase again slightly at 60% strain (Figures 4c and 4g), the anisotropy is maintained (Figure 5c).

4.3. Microscopic Analysis: Pore Compaction Versus Cracking

Microscopic and micro-CT analysis shows that the brittle and viscous components of strain differ for each material (Figure 6 and Movies S1–S6 in the supporting information). The degree of cracking, and crack opening, considering the relatively low applied stress conditions, is remarkable. Crack width (dimension of maximum opening of the crack) and length (maximum dimension parallel to core axis, i.e., in the *z* axis) are described here. In crystal-poor NP, cracks propagate between pores, primarily parallel to the main compressive stress. Large cracks (~0.06 mm maximum aperture) not present initially (Figure 6a) or in the early

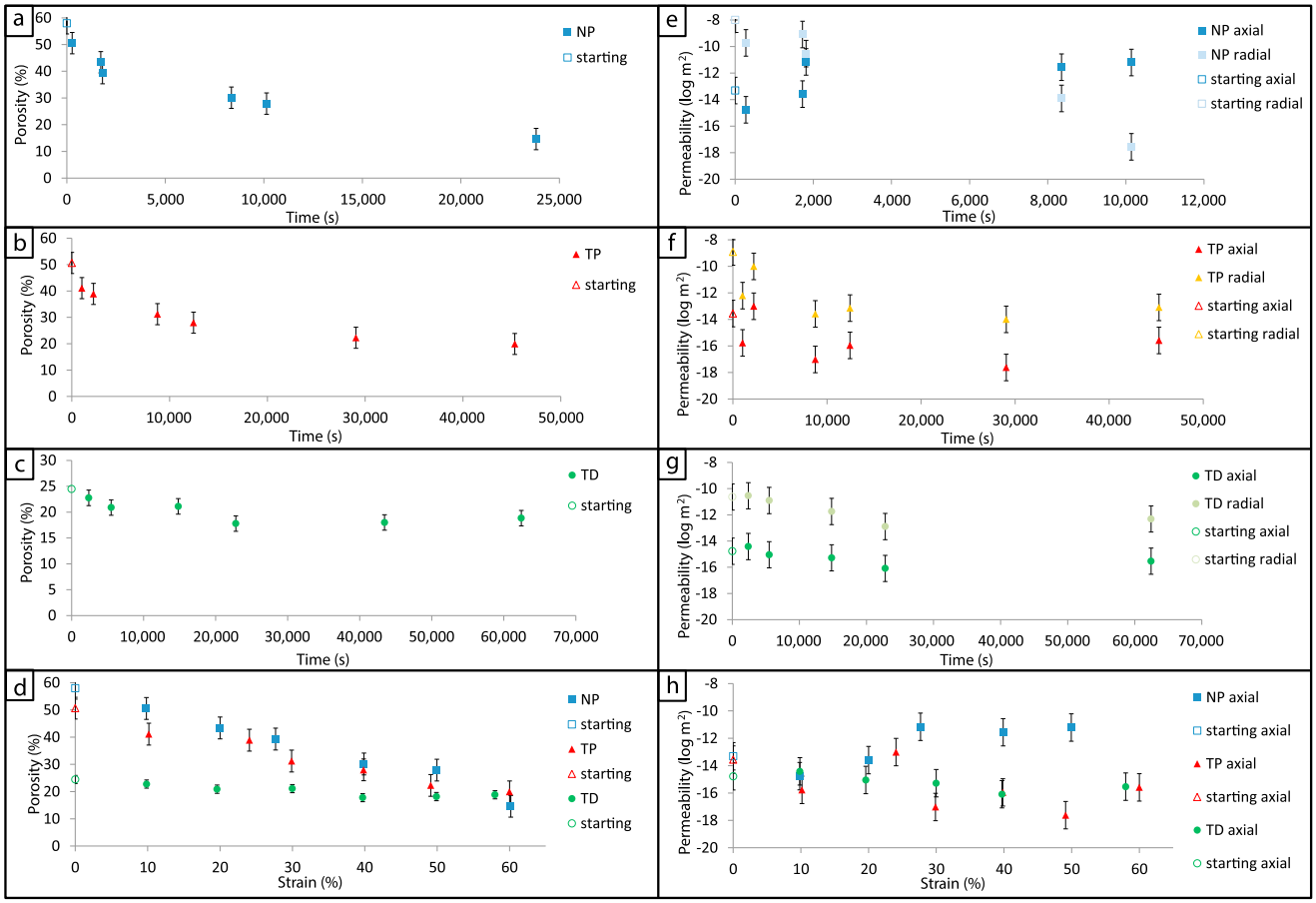

Figure 4. Structural evolution in lavas which have been experimentally compacted. Porosity change up to 60% strain for (a) sample NP, (b) sample TP, (c) sample TD as a function of time, and (d) all samples as a function of strain. The uncertainty of porosity measurements is $< 4\%$. Axial and radial permeability change for (e) sample NP up to 50% strain, (f) sample TP up to 60% strain, (g) sample TD up to 60% strain (missing 50%), and (h) axial permeability evolution as a function of strain. The uncertainty of the permeability measurements is 1 log unit.

stages of compaction (Figure 6b) develop across half the length of the sample by 20% strain (Figure 6c). These cracks propagate further and widen (~0.12 mm maximum aperture) with increased strain (60%; Figure 6d), concurrent with the increasing axial permeability during compaction for the crystal-poor sample (Figure 5a). Crystal-rich lavas TP and TD initially contain a higher proportion of microcracks, especially in crystals, than sample NP (Figures 6e and 6i). Deformation induces more fractures in phenocrysts and in the adjacent melt as crystals are pulverized, especially at high strains when crystals begin to interact with one another. Short but wide radial cracks form perpendicular to the applied axial stress direction (e.g., Figure 6g): the cracks achieve a width of 0.05 mm by 20% strain in TP and 0.1 mm by 60% (Figure 6l) in TD. Cracks initiated in crystals tend to propagate laterally into melt, and those formed in the melt terminate or deflect as they encounter phenocrysts; hence, their length does not compare to those produced in crystal-poor NP and as such do not have a dominant influence on permeability anisotropy (Figures 5b and 5c). Ultimately, even the largest cracks have a jagged profile across the phenocrysts and glass due to en echelon fracture propagation events in and adjacent to crystals, and deflection of propagating cracks around phenocrysts, whereas the cracks in NP were hindered by fewer obstacles (Movies S4–S6).

Compaction also strongly affected the shape of vesicles (which are preexisting and are hereafter referred to as "pores" and excludes open space created by cracks), with large pores collapsing quickly in all samples, whereas small pores remained mostly undeformed (Figure 6 and Movies S4–S6). Analysis of a coalesced pore cluster in NP shows a drastic reduction in pore size (Figure 7). The collapsed porous structures are occasionally in filled with fractured pore wall shards or fragments of pulverized adjacent crystals (e.g., Figure 6k). In the vicinity of crystals, pores remain largely intact, although size is reduced (Figure 7).

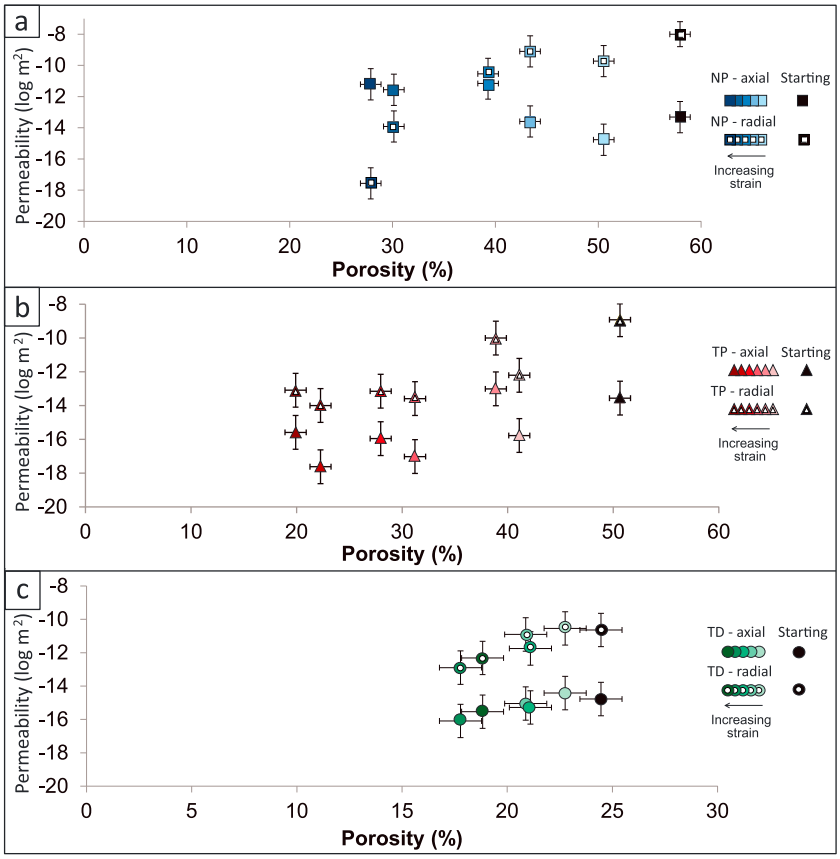

Figure 5. Axial and radial permeability evolution with porosity as a function of strain for (a) sample NP to up to 50% strain, showing initial anisotropy and a reversal in anisotropy after 30% strain, (b) sample TP up to 60% strain, and (c) sample TD up to 60% strain (missing 50%) both showing concurrent decrease in both axial and radial permeability (anisotropy is maintained). Uncertainty of the values of change in porosity and permeability is double that shown in Figure 4 for both measurements.

In all samples, preexisting pores (even those protected by crystals) are shortened in a direction parallel to the principle stress direction, while cracks are lengthened; porosity is reduced; crystals are fractured; the strain rate reduced, and viscosity increased due to strain hardening. Permeability decreased, maintaining similar permeability anisotropies, except in the crystal-poor sample where axially orientated cracking occurred, concordant to an absolute and relative increase in axial permeability.

5. Interpretation

5.1. The Rheology of Compacting Porous Lavas

The contrasting physical behavior of the samples can be attributed to characteristic styles of deformation associated with pore collapse and crack propagation (Movies S1–S6). At the onset of compaction, high initial strain rates, on the fragile porous samples induces cracking of pore walls as recorded by released AEs (Figure 2); this causes the largest pores to collapse, rapidly reducing the net porosity of the samples (Figures 4a–4c). This densification causes strain hardening as the magma properties evolve, which is manifested as a nonlinear increase in the apparent viscosity and equivalent nonlinear decrease in the compaction strain rate (Figure 3), an observation in agreement with previous compaction studies [*Quane et al*., 2009]. The initial closure of the largest pores increases the apparent viscosity due to densification, decreases the strain rate, and reduces the amount of cracking in the later stages of compaction (Figure 2). This decrease occurs as viscous flow (and phenocryst pulverization in the interacting crystal framework) becomes the dominant deformation mechanism, similar to the nonproportional decrease in AE observed by *Lavallée et al*. [2008] with a decrease in strain rate. The closure of pores is thought to be largely

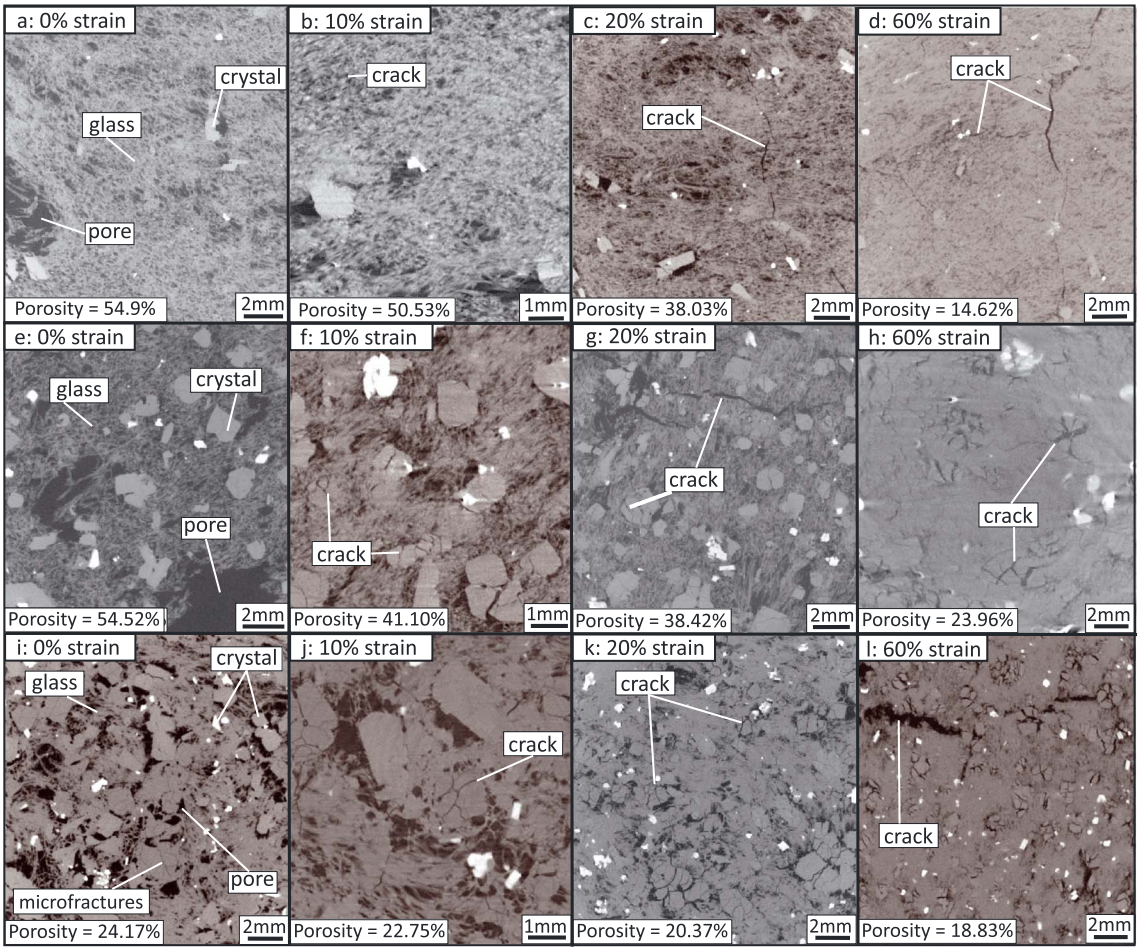

Figure 6. Tomography images (in *X-Y* dimensions) from undeformed (0%), 10, 20, and 60% strain samples from the center of samples of NP, TP, and TD. Primary stress direction is into the page (i.e., *Z* dimension).

accommodated in the connected network where pores are unable to pressurize in response to applied stresses and instead simply outgas, allowing the remnant melt to flow into and close them.

The apparent viscosities of the compacting lavas evolve differently depending on the initial crystal and pore fractions. The crystal-rich, lowest porosity sample (TD) was most viscous, and the crystal-poor, highest-porosity sample (NP) was the least viscous. For all samples strain hardening was evident: apparent and relative viscosity increased by approximately one order of magnitude from 0 to 50% strain as a result of densification. Further investigation confirms that crystals increase the apparent viscosity; TP exhibits a higher viscosity than the crystal-poor NP (with similar porosities; Figure 3d), consistent with previous findings on crystal-bearing suspensions [*Caricchi et al.*, 2007; *Lavallée et al.*, 2007; *Mueller et al.*, 2011]. In addition, we see that connected pores decrease the apparent viscosity; NP has an unexpectedly low initial viscosity (Figure 3d), and the comparison of TD with TP shows that the denser sample has higher relative viscosity, consistent with previous results [e.g., *Pistone et al.*, 2012]. Upon compaction the apparent and relative viscosity increases rapidly up to >5% strain for all samples. More compaction leads to a further increase in viscosity, which is concordant for the samples with similar high porosities (NP and TP) and slower for the denser TD. Although the porosities and strain rates of the crystal-rich TP and TD converge at 50% strain, the viscosities remain contrasting, likely due to the slightly higher crystal content of TD. The dynamics of deformation of these lavas is a function of the experimental conditions used. In the natural environment, small local changes in temperature and water content will severely affect melt viscosity [*Hess and Dingwell*, 1996], and/ or variation in simple shear (rotational deformation) and confining pressure will together result in different porosity thresholds and deformation styles, but the findings here are consistent with a highly transient rheology as porous lavas are forced to compact.

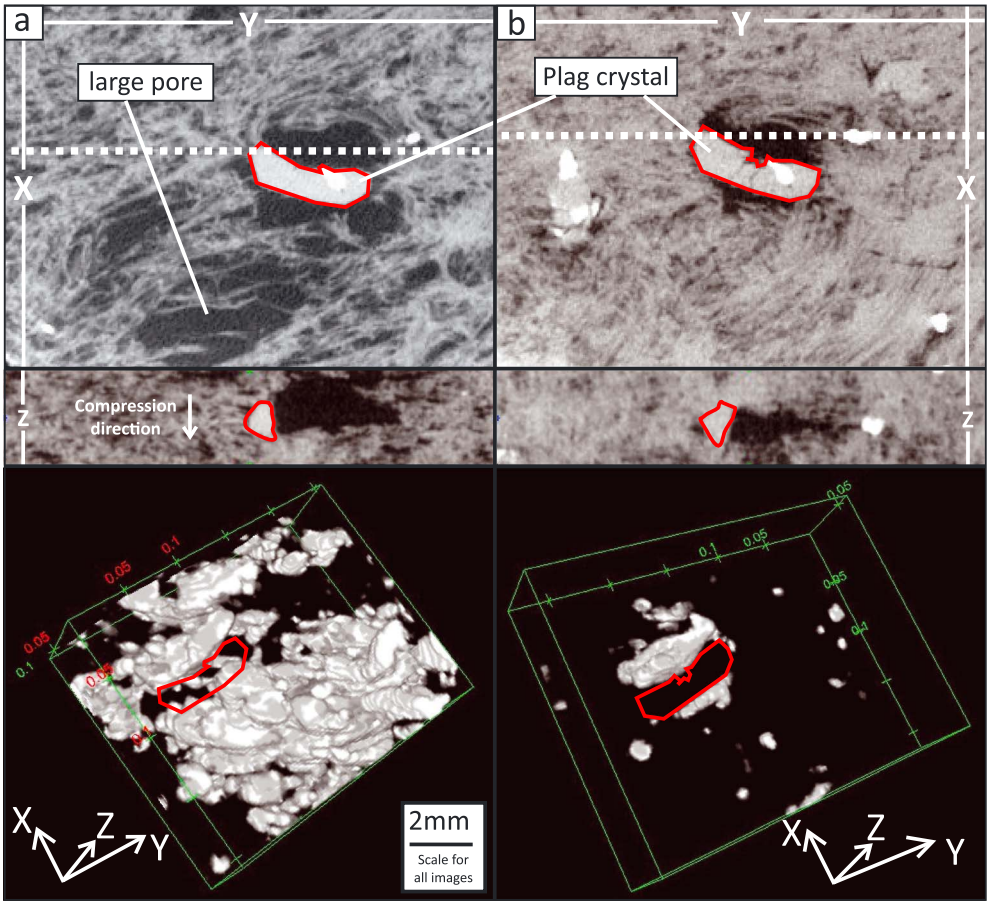

Figure 7. Pore shape and size changes in NP between 0% and 60% axial strain. *XY* (perpendicular to compression direction) and *YZ* (parallel to compression direction slices shown (*YZ* slices correspond to dashed white line)). (bottom row) Three-dimensional image of pores above 30 μm with position of plagioclase crystal shown for reference.

5.2. Permeability of Compacting Porous Lavas

The densification of crystal-poor and crystal-rich porous lavas results in contrasting permeability scenarios. In crystal-poor lava NP, the compaction of large pores and anisotropic propagation of cracks axially through the foam causes permeability parallel to the principal stress to increase, whereas permeability decreases perpendicular to the principal stress (radially in the sample). The comparatively high occurrence of cracking events at the onset of compaction suggests brittle vesicle wall collapse, in addition to vesicle wall bending and buckling resulting in closure of the largest pores. Closure of pores explains the decreasing radial permeability, whereas the progressive opening of early cracks (along with new crack nucleation and propagation) has an important contribution to the continuous increase in axial permeability in the crystal-poor NP sample (Figures 4 and 5). This finding supports the conclusion that reduction in permeability by compaction may be thwarted by the production of cracks working to channel gas flow in crystal-poor lava.

However, where a higher proportion of crystals exist, permeability is reduced simultaneously both axially and radially in samples TP and TD until 50% strain, after which porosity and permeability are slightly increased in TD, and permeability increases in TP. In contrast to low crystallinity NP, permeability anisotropy is maintained throughout compaction in higher crystallinity samples. Fractures tend to be confined to crystals until higher strains and densification is inhibited by the solid fraction, which limits the reduction in both porosity and permeability. The overall short and multidirectional cracks do not enforce a strong control on the permeability evolution, which is dominated by viscous pore closure. Sparse propagation of cracks across the samples at the highest strains counteracts permeability decrease, working in competition against compaction. The impact of uniaxial strain on the permeability anisotropy suggests that high total

strain is required to construct or modify an anisotropic permeable structure under compaction, although shearing, which is of great importance during conduit transport of magma, can reduce porosity further and strongly influence permeability anisotropy [e.g., *Shields et al*., 2014]. Thus, our analysis is consistent with a view in which the evolution of the permeability of porous lava structures during compaction is specific to the spatially variable initial textures of the dome, the load applied, and the range of strain experienced.

6. Discussion

6.1. Rheology of Porous and Crystal-Bearing Magma

The effect of crystals and pores on the rheology of magma has been the subject of numerous experimental studies [*Bagdassarov and Dingwell*, 1993; *Lejeune et al*., 1999; *Llewellin and Manga*, 2005; *Caricchi et al*., 2007; *Lavallée et al*., 2007; *Cordonnier et al*., 2009; *Costa et al*., 2009; *Quane et al*., 2009; *Cimarelli et al*., 2011; *Picard et al*., 2011; *Avard and Whittington*, 2012; *Pistone et al*., 2012; *Kendrick et al*., 2013; *Mader et al*., 2013 and references therein; *Okumura and Sasaki*, 2014; *Shields et al*., 2014] and is used widely in numerical simulations [e.g., *Melnik et al*., 2005; *Ittai et al*., 2010; *Deubelbeiss et al*., 2011]. For systems in which pores are isolated and suspended in a continuous melt (i.e., bubbles), their deformability is dependent on their size for a given local shear rate and melt phase. If bubbles are deformable (which is true for large bubbles), the bulk viscosity of a suspension is decreased [*Manga et al*., 1998; *Rust and Manga*, 2002]. However, the effect of interconnected pore networks, such as those found in the samples used here, on rheology remains underexplored. We show that pore networks which are interconnected to the edges of samples (i.e., compressible) must be highly deformable and therefore, are likely to decrease suspension viscosity and allow the system to behave as a compacting column. This explains the initially low calculated relative viscosity of crystal-poor NP, which is initially lower than the predicted melt viscosity at the experimental temperature. Because the strain rates resulting from the applied stress are far below those at which silicate melts will become shear thinning [*Webb and Dingwell*, 1990] and because the crystal content is very low, we propose that the relative viscosity below 1 is due to the suspension effect of the interconnected pores.

Quane et al. [2009] and *Quane and Russell* [2005] showed that porosity loss during compaction of a sintered ash aggregate (a connected porous structure) induced a nonlinear strain-dependent increase in apparent viscosity. Our findings are similar to those of *Quane et al*. [2009], showing an initially high strain rate and increase in apparent and, thus, relative viscosity as porosity is removed by compaction (i.e., strain hardening). *Quane and Russell* [2005] linked strain-dependent porosity to a measurable initial melt viscosity, initial total porosity, and the applied stress via an empirically determined term α. This empirical factor likely represents unmeasured aspects of the pore network geometry and interconnectivity and their evolution with time. The magnitude of α for our experiments would be different than for the sintered ash aggregate or the glass bead packs presented in *Quane and Russell* [2005] due to the additional complexities presented by crystal-bearing rheology and the different pore geometries in our samples. We opt not to model α here because equation (1) permits us to make direct observations of the apparent viscosity and how it evolves with strain.

Deformation of porous lavas can occur by compaction (which involves the successive removal of a phase in the system until that phase is exhausted) or by simple shear of a suspension of isolated pores (in which the phases are all suspended and variably deform and reorganize in flow). When the interconnected pore phase is depleted (something not achieved in our experiments), the physics of the flow may be encapsulated by models for isolated bubble and crystal suspension rheology. However, compaction is the transient phase before steady flow can be achieved, and this portion of deformation in highly viscous magmatic systems is investigated here.

Deformation of porous lavas (up to 60% strain) results in densification to no less than a threshold of 17–19% pores in crystal-rich samples, caused in part by the abundance of pressure shadows around crystals and isolation of pores. In crystal-poor samples, a lower, unknown porosity threshold might exist beyond 60% strain but was not achieved in our experiments. Closure of noncrack-related pores increases the density of the system, decreasing the abundance of local stress concentration at the pore walls and causing strain hardening to produce an apparently stiffer suspension. Fractures form at high strain rates (Figure 6) but do not cause strain weakening behavior observed at higher stresses in other studies

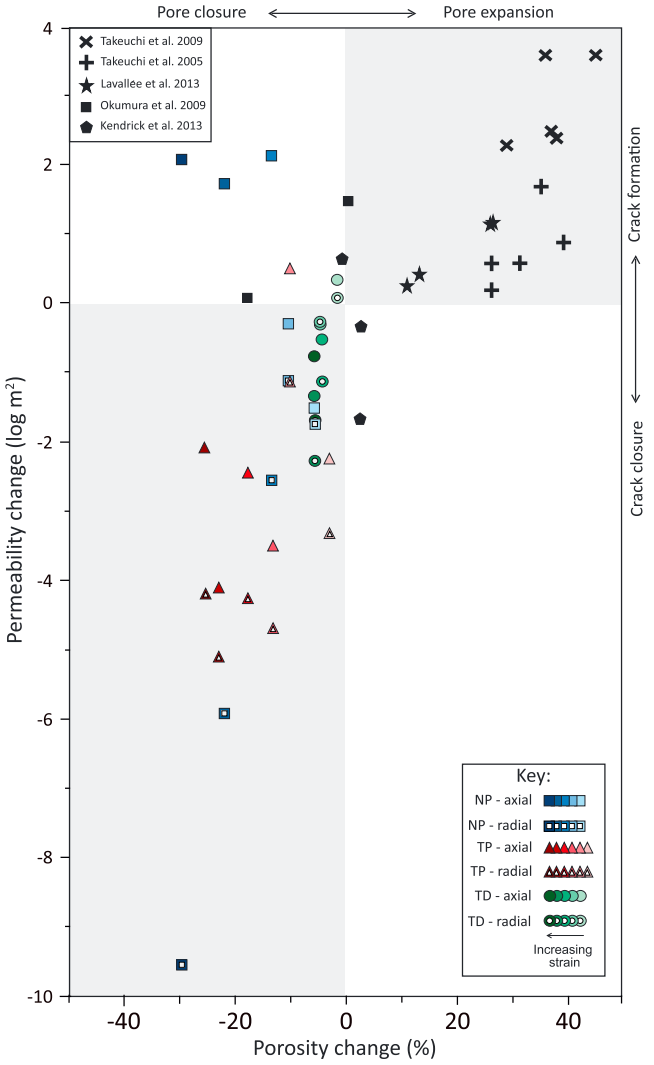

Figure 8. Relationship between connected porosity and permeability for compression and vesiculation experiments in lavas. Colors are from this study; black shapes denote previously published work, all of which were direct measurements, except for *Lavallée et al.* [2013] which were estimated from the reconstructed porosity via the relationship $k = 10^{-17}\Phi^{3.4}$ from *Mueller et al.* [2005].

on crystal-bearing magmas [e.g., *Kendrick et al.*, 2013], instead the magmas deform viscously, conforming to non-Newtonian rheology typical of three-phase magmatic suspensions [e.g., *Lavallée et al.*, 2007, 2008, 2013].

6.2. Permeability Evolution of Porous Magma

The permeability of a porous magma can control transitions between explosive and effusive eruptions [e.g., *Mueller et al.*, 2005; *Kolzenburg et al.*, 2012]. Studies of natural samples have shown that permeability relates to porosity [e.g., *Mueller et al.*, 2005, 2008; *Okumura et al.*, 2009; *Wright et al.*, 2009]. Recent experimentation has shown that stress, strain rate, strain, melt viscosity, crystallinity, and vesicularity affect the construction of the permeable porous network (see Figure 8; with further information in *Okumura et al.* [2009], *Burgisser and Gardner* [2004], *Laumonier et al.* [2011], *Kendrick et al.* [2013], and *Lavallée et al.* [2013]), but a complete description of the competing factors still eludes us.

Foaming experiments have shown that during pore growth, increasing coalescence increases the foam permeability by several orders of magnitude (Figure 8) [*Takeuchi et al.*, 2005, 2009]. In contrast, low strain rate torsional experiments on crystal-poor rhyolitic foam have shown that a moderate 33% shear strain induces only a relatively small change in porosity, despite a significant increase in lateral permeability of nearly 2 orders of magnitude due to pore elongation (Figure 8) [*Okumura et al.*, 2009]. *Lavallée et al.* [2013] showed that deformation of dense crystal-rich andesitic lavas at high stresses (28 to 76 MPa) across the viscous to brittle transition induces enough localized cracking to produce a large increase in porosity (up to 30%), estimated to induce an increase in permeability and its anisotropy (Figure 8). Complementary experiments at lower stresses (2.8 to 24 MPa) showed that disperse microcracking can generate similar decreases in permeability due to rearrangement of porosity [*Kendrick et al.*, 2013]. This range of observations in all the experimental work to date can be ascribed to a competition between (A) compacting or opening pores (vesicles) and (B) compacting or opening cracks (Figure 8). Pores open and close causing large changes in porosity but lesser changes in permeability, in contrast with opening and closing of cracks, which have far greater an effect on permeability than porosity. Therefore, the propagation direction in Figure 8 can be used to imply the basic mechanisms of textural evolution.

Our samples showed a complex evolution and interplay of porosity and permeability. Compaction decreased porosity down to 17–19% irrespective of starting porosity for the crystal-rich magmas, although

the initially denser TD sample achieved this target at lower total strain (40–50% compared to 50–60% for the porous sample TP). It is likely that the crystal-poor sample (NP) would continue to compact to a lower porosity threshold than the 14% observed here with further strain (see *Vasseur et al*. [2013] and *Wadsworth et al*. [2014] for more information). Permeability evolution was more complex, however: as the crystal-rich TP and TD densified, permeability reduced both axially and radially (until a slight increase occurred at 60% strain) and the anisotropy was maintained throughout; in the crystal-poor NP, radial permeability decreased similarly to the crystal-rich samples, but axial permeability increased rapidly with strain, and the permeability anisotropy was reversed beyond 30% strain due to the influence of axially propagating cracks.

The behavior of samples TP and TD suggests that the short, crystal-confined or crystal-terminated cracks forming in crystal-rich lavas during compaction will not overcome the reduction in permeability from closure of the pores and a net reduction of porosity (Figures 4 and 7). In the crystal-poor NP sample, large increases in axial permeability occurred despite a significant decrease in porosity due to the formation of long cracks that dominated the permeable network. We conclude that during compaction at low stresses, porosity will be reduced, but permeability evolution will be dictated by the original crystal content (and probably to a lesser degree, the crystal size distribution, though not investigated here) of the magma.

7. Implications for Volcanic Systems

Large proportions of lava domes may be subject to near-uniaxial deformation, as their margins are permitted to expand laterally. The stress in this scenario is imposed by the overburden (depth within dome) and ascent of magma below. The range of porosity in lava domes (this study and see also *Kueppers et al*. [2005], *Mueller et al*. [2011], and *Lavallée et al*. [2013]) and the tendency for the deeper central part of the dome to be denser than the outer carapace [e.g., *Fink et al*., 1992] suggest that the compaction process presented herein contributes to porosity reduction. Although, we note that some variation in porosity can be attributed to in situ bubble growth [*Fink et al*., 1992]. Structurally, the role of compaction is supported by the presence of compressed (i.e., elongate) pores in the vesicular dome rocks and localized shear bands in the dense dome rocks. Compaction tests of the dome lavas presented here suggest that porosity reduction, although approximately proportional to strain until a threshold, would slow through time (provided that the acting forces remain constant), while modifying the permeable porous network. Our results suggest that outgassing through vertical cracks within a lava dome (perpendicular to flow-orientated bubbles) is more efficient than through the anisotropic bubble network, which is gradually closed during compaction. The experiments reveal contrasting permeability evolution in crystal-poor versus crystal-rich lavas, with cracks more readily able to propagate in the crystal-poor system. Permeability changes influence outgassing ability and thus regulate the likelihood of effusive-explosive eruption transitions in active lava domes.

Cracks produced by compaction locally affect permeability of the foam; yet their potential ability to bleed pore pressure is only as great as their pervasive extent across the dome and upper conduit (such as tuffisites described by *Berlo et al*. [2013] and *Castro et al*. [2012b]). As much as cracks can locally decrease the pore pressure and seemingly decrease the likelihood of an explosive event [e.g., *Mueller et al*., 2011], cracks produced during foam compaction form zones of weakness [e.g., *Kendrick et al*., 2013] that can eventually grow to such extent that they may connect highly pressurized regions of the conduit to the atmosphere, thereby causing a pressure gradient that may trigger the fragmentation of the deep magma [e.g., *Spieler et al*., 2004] or bleed overpressure from an inadequately connected pore network [e.g., *Schipper et al*., 2013], leading to episodic explosions superimposed onto degassing through permeable networks [e.g., *Castro et al*., 2014].

Our experiments show that the permeability of lava domes will change over time as pores close and cracks nucleate, propagate, coalesce, and heal as a large (150+ m thick) lava dome compacts under its own weight. Changes in permeability and permeability anisotropy are strongly affected by crystal content: crystalline lavas experience greater permeability reduction under the same strain conditions and could therefore be more prone to pressure accumulation that drives explosive eruptions. Hence, this is an important consideration when assessing the ability for a growing lava dome to outgas or potential to fragment and erupt explosively.

8. Conclusions

Uniaxial compression experiments were performed to investigate the mechanics by which the permeable porous network of dome lavas evolves during compaction at low stresses. The experiments show the following:

1. Pores compact by pore wall failure and viscous flow and partial infill by crystal and glass fragments.
2. Compaction of porous lava under a constant stress results in a nonlinear decrease in porosity, decrease in strain rate (cf. compaction rate), and resultant increase in apparent and relative viscosity that results from strain hardening.
3. Pumiceous crystal-poor lavas have a lower apparent and relative viscosity and consequently experience the highest strain rates of the experiments presented here. The presence of connected porosity decreases viscosity, and during compaction large pores rapidly close and pervasive cracks simultaneously form as recorded by acoustic emissions. Compaction induces a progressive decrease of radial permeability due to viscous pore deformation and an increase in axial permeability due to crack propagation parallel to the principal stress axis, thus reversing the initial anisotropy of the permeable network.
4. Crystal-rich lavas have a higher apparent viscosity and experience a lower strain rate than the crystal-poor lava. The initial difference between the denser and more porous crystal-rich lava is negated as strain increases and porosity becomes similar in both. Pores compact in a similar manner as in crystal-poor samples, but cracking events registered by acoustic emissions are due to abundant short cracks propagating within the crystal phase. The presence of crystals also hinders pore compaction, forming pressure shadows. The permeability decreases significantly both axially and radially until ~50% strain, beyond which cracking begins to compete with viscous pore deformation and permeability stabilizes, yet the anisotropy remains constant during compaction.
5. Crystal-rich samples achieve a threshold porosity of 17–19%, beyond which continued strain is unable to further compact and barreling and vertical fractures take over. This threshold is reached at lower strain for the initially denser sample (TD). In the crystal-poor sample, an unknown, lower porosity threshold is likely to be met at strain beyond 60% but was not achieved in these experiments.

We conclude that the inherent permeability of lava domes can be partially explained by cracking during the compaction process even at low stress. Cracking counteracts porous network closure, and compaction alone is insufficient to completely close the permeable porous network. This may allow compacting lava domes to outgas along localized permeable cracks. This deformation regime is relevant to lava domes, but we recommend exercising caution when applying this lava dome analogy to magma in conduits, where higher magmastatic and confining pressure regimes and shear stress fields dominate.

Acknowledgments

The authors wish to thank H. Tuffen and H. Wright for constructive reviews of this manuscript. We also wish to acknowledge the International Bureau of the Federal Ministry of Education and Science and Research (BMBF in Germany), the International Science and Technology (ISAT) Linkages Fund (in New Zealand) for an international cooperation grant, the European Research Council for the Starting Grant on "Strain Localisation in Magmas" (SLiM, 306488), the Advanced Grant on "Explosive Volcanism in the Earth System: Experimental Insights" (EVOKES, 247076), the European Union's Seventh Programme for Research, Technological Development and Demonstration under grant agreement 282759 (VUELCO), and the Marsden Fast Start for project "Uncorking volcanoes —the textural evolution of volcanic plugs" (09-UO-017C). Part of this work was undertaken on the IM Beamline at the Australian Synchrotron, Victoria, Australia. The Earthquake Commission of New Zealand, GNS Science, Mason Trust Fund, and Mighty River Power Ltd. are also acknowledged for funding of P. Ashwell. We would also like to thank Ken Raureti and the members of the Ruawahia 2B Trust for access to Ruawahia. Please contact the corresponding author for access to the raw data that this study is based upon.

References

Ashwell, P. A. (2014), Controls on rhyolite lava dome eruptions in the Taupo Volcanic Zone, PhD thesis, Department of Geological Sciences, Univ. of Canterbury, New Zealand.

Ashwell, P. A., B. M. Kennedy, D. M. Gravley, F. W. von Aulock, and J. W. Cole (2013), Insights into caldera and regional structures and magma body distribution from lava domes at Rotorua Caldera, New Zealand, *J. Volcanol. Geotherm. Res.*, *258*, 187–202.

Avard, G., and A. G. Whittington (2012), Rheology of arc dacite lavas: Experimental determination at low strain rates, *Bull. Volcanol.*, *74*(5), 1039–1056.

Bagdassarov, N. S., and D. B. Dingwell (1993), Deformation of foamed rhyolites under internal and external stresses: An experimental investigation, *Bull. Volcanol.*, *55*, 147–154.

Berlo, K., H. Tuffen, V. C. Smith, J. M. Castro, D. M. Pyle, T. A. Mather, and K. Geraki (2013), Element variations in rhyolitic magma resulting from gas transport, *Geochim. Cosmochim. Acta*, *121*, 436–451.

Bouvet de Maisonneuve, C., O. Bachmann, and A. Burgisser (2009), Characterization of juvenile pyroclasts from the Kos Plateau Tuff (Aegean Arc): Insights into the eruptive dynamics of a large rhyolitic eruption, *Bull. Volcanol.*, *71*(6), 643–658.

Burgisser, A., and J. E. Gardner (2004), Experimental constraints on degassing and permeability in volcanic conduit flow, *Bull. Volcanol.*, *67*(1), 42–56.

Cabrera, A., R. F. Weinberg, H. M. N. Wright, S. Zlotnik, and R. A. F. Cas (2011), Melt fracturing and healing: A mechanism for degassing and origin of silicic obsidian, *Geology*, *39*(1), 67–70.

Caricchi, L., L. Burlini, P. Ulmer, T. Gerya, M. Vassalli, and P. Papale (2007), Non-Newtonian rheology of crystal-bearing magmas and implications for magma ascent dynamics, *Earth Planet. Sci. Lett.*, *264*(3–4), 402–419.

Caricchi, L., A. Pommier, M. Pistone, J. Castro, A. Burgisser, and D. Perugini (2011), Strain-induced magma degassing: insights from simple-shear experiments on bubble bearing melts, *Bull. Volcanol.*, *73*(9), 1245–1257.

Cashman, K. V., and R. S. J. Sparks (2013), How volcanoes work: A 25 year perspective, *Geol. Soc. Am. Bull.*, *125*(5–6), 664–690.

Cashman, K. V., B. Sturtevant, P. Papale, O. Navon, and R. D. Ballard (2000), Magmatic fragmentation, in *Encyclopedia of Volcanoes*, edited by H. Sigurdsson et al., pp. 421–431, Academic Press, San Diego, Calif.

Cashman, K. V., C. R. Thornber, and J. S. Pallister (2008), From dome to dust: Shallow crystallization and fragmentation of conduit magma during the 2004–2006 dome extrusion of Mount St. Helens, Washington, in *A Volcano Rekindled: The Renewed Eruption of Mount St. Helens, 2004–2006*, edited by D. R. Sherrod, W. E. Scott, and P. H. Stauffer, *U.S. Geol. Surv. Prof. Pap.*, *1750*, pp. 387–413.

Castro, J. M., A. Burgisser, C. I. Schipper, and S. Mancini (2012a), Mechanisms of bubble coalescence in silicic magmas, *Bull. Volcanol.*, *74*(10), 2339–2352.

Castro, J. M., B. Cordonnier, H. Tuffen, M. J. Tobin, L. Puskar, M. C. Martin, and H. A. Bechtel (2012b), The role of melt-fracture degassing in defusing explosive rhyolite eruptions at volcán Chaitén, *Earth Planet. Sci. Lett.*, *333–334*, 63–69.

Castro, J. M., I. N. Bindeman, H. Tuffen, and C. Ian Schipper (2014), Explosive origin of silicic lava: Textural and –H2O evidence for pyroclastic degassing during rhyolite effusion, *Earth Planet. Sci. Lett.*, *405*, 52–61.

Cimarelli, C., A. Costa, S. Mueller, and H. M. Mader (2011), Rheology of magmas with bimodal crystal size and shape distributions: Insights from analog experiments, *Geochem. Geophys. Geosyst.*, *12*, Q07024, doi:10.1029/2011GC003606.

Cole, J. W. (1970), Structure and eruptive history of the Tarawera Volcanic Complex, *N. Z. J. Geol. Geophys.*, *13*(4), 881–902.

Collinson, A. S. D., and J. W. Neuberg (2012), Gas storage, transport and pressure changes in an evolving permeable volcanic edifice, *J. Volcanol. Geotherm. Res.*, *243–244*, 1–13.

Cordonnier, B., K.-U. Hess, Y. Lavallée, and D. B. Dingwell (2009), Rheological properties of dome lavas: Case study of Unzen volcano, *Earth Planet. Sci. Lett.*, *279*(3–4), 263–272.

Costa, A., L. Caricchi, and N. Bagdassarov (2009), A model for the rheology of particle-bearing suspensions and partially molten rocks, *Geochem. Geophys. Geosyst.*, *10*, Q03010, doi:10.1029/2008GC002138.

Deubelbeiss, Y., B. J. P. Kaus, J. A. D. Connolly, and L. Caricchi (2011), Potential causes for the non-Newtonian rheology of crystal-bearing magmas, *Geochem. Geophys. Geosyst.*, *12*, Q05007, doi:10.1029/2010GC003485.

Dingwell, D., and S. L. Webb (1989), Structural relaxation in silicate melts and Non-Newtonian melt rheology in geologic processes, *Phys. Chem. Miner.*, *16*, 508–516.

Edmonds, M., and R. A. Herd (2007), A volcanic degassing event at the explosive-effusive transition, *Geophys. Res. Lett.*, *34*, L21310, doi:10.1029/2007GL031379.

Fink, J. H., S. W. Anderson, and C. R. Manley (1992), Textural constraints on effusive silicic volcanism: Beyond the permeable foam model, *J. Geophys. Res.*, *97*(B6), 9073–9083, doi:10.1029/92JB00416.

Gaunt, H. E., P. R. Sammonds, P. G. Meredith, R. Smith, and J. S. Pallister (2014), Pathways for degassing during the lava dome eruption of Mount St. Helens 2004–2008, *Geology*, *42*, 947–950.

Gent, A. N. (1960), Theory of the parallel plate viscometer, *Br. J. Appl. Phys.*, *11*(2), 85–87.

Giordano, D., J. K. Russell, and D. B. Dingwell (2008), Viscosity of magmatic liquids: A model, *Earth Planet. Sci. Lett.*, *271*(1–4), 123–134.

Hale, A. J., and G. Wadge (2008), The transition from endogenous to exogenous growth of lava domes with the development of shear bands, *J. Volcanol. Geotherm. Res.*, *171*(3–4), 237–257.

Herd, R. A., M. Edmonds, and V. A. Bass (2005), Catastrophic lava dome failure at Soufrière Hills Volcano, Montserrat, 12–13 July 2003, *J. Volcanol. Geotherm. Res.*, *148*(3–4), 234–252.

Hess, K. U., and D. B. Dingwell (1996), Viscosities of hydrous leucogranitic melts: A non-Arrhenian model, *Am. Mineral.*, *81*(9–10), 1297–1300.

Hess, K.-U., B. Cordonnier, Y. Lavallée, and D. B. Dingwell (2007), High-load, high-temperature deformation apparatus for synthetic and natural silicate melts, *Rev. Sci. Instrum.*, *78*(7), 075102.

Hess, K.-U., B. Cordonnier, Y. Lavallée, and D. B. Dingwell (2008), Viscous heating in rhyolite: An in situ experimental determination, *Earth Planet. Sci. Lett.*, *275*(1–2), 121–126.

Holland, A. S. P., I. M. Watson, J. C. Phillips, L. Caricchi, and M. P. Dalton (2011), Degassing processes during lava dome growth: Insights from Santiaguito lava dome, Guatemala, *J. Volcanol. Geotherm. Res.*, *202*(1–2), 153–166.

Humphreys, M. C. S., T. Menand, J. D. Blundy, and K. Klimm (2008), Magma ascent rates in explosive eruptions: Constraints from H2O diffusion in melt inclusions, *Earth Planet. Sci. Lett.*, *270*(1–2), 25–40.

Ittai, K., L. Vladimir, and N. Oded (2010), Bubble growth in visco-elastic magma: Implications to magma fragmentation and bubble nucleation, *Bull. Volcanol.*, *73*(1), 39–54.

Johnson, J. B., J. M. Lees, A. Gerst, D. L. Sahagian, and N. Varley (2008), Long-period earthquakes and co-eruptive dome inflation seen with particle image velocimetry, *Nature*, *456*(7220), 377–81.

Kendrick, J. E., Y. Lavallée, K.-U. Hess, M. J. Heap, H. E. Gaunt, P. Meredith, and D. B. Dingwell (2013), Tracking the permeable porous network during strain-dependent magmatic flow, *J. Volcanol. Geotherm. Res.*, *260*, 117–126.

Kendrick, J. E., Y. Lavallée, K. U. Hess, S. De Angelis, A. Ferk, H. E. Gaunt, P. G. Meredith, D. B. Dingwell, and R. Leonhardt (2014), Seismogenic frictional melting in the magmatic column, *Solid Earth*, *5*(1), 199–208.

Kennedy, B. M., A. M. Jellinek, J. K. Russell, A. R. L. Nichols, and N. Vigouroux (2010), Time-and temperature-dependent conduit wall porosity: A key control on degassing and explosivity at Tarawera volcano, New Zealand, *Earth Planet. Sci. Lett.*, *299*(1–2), 126–137.

Klug, C., and K. V. Cashman (1996), Permeability development in vesiculating magmas: Implications for fragmentation, *Bull. Volcanol.*, *58*, 87–100.

Kolzenburg, S., M. J. Heap, Y. Lavallée, J. K. Russell, P. G. Meredith, and D. B. Dingwell (2012), Strength and permeability recovery of tuffisite-bearing andesite, *Solid Earth*, *3*, 191–198.

Kueppers, U., B. Scheu, O. Spieler, and D. B. Dingwell (2005), Field-based density measurements as tool to identify preeruption dome structure: Set-up and first results from Unzen volcano, Japan, *J. Volcanol. Geotherm. Res.*, *141*(1–2), 65–75.

Laumonier, M., L. Arbaret, A. Burgisser, and R. Champallier (2011), Porosity redistribution enhanced by strain localization in crystal-rich magmas, *Geology*, *39*(1), 715–718.

Lavallée, Y., K.-U. Hess, B. Cordonnier, and D. B. Dingwell (2007), Non-Newtonian rheological law for highly crystalline dome lavas, *Geology*, *35*(9), 843–846.

Lavallée, Y., P. G. Meredith, D. B. Dingwell, K.-U. Hess, J. Wassermann, B. Cordonnier, A. Gerik, and J. H. Kruhl (2008), Seismogenic lavas and explosive eruption forecasting, *Nature*, *453*, 507–510.

Lavallée, Y., T. M. Mitchell, M. J. Heap, J. Vasseur, K.-U. Hess, T. Hirose, and D. B. Dingwell (2012), Experimental generation of volcanic pseudotachylytes: Constraining rheology, *J. Struct. Geol.*, *38*, 222–233.

Lavallée, Y., P. M. Benson, M. J. Heap, K.-U. Hess, A. Flaws, B. Schillinger, P. G. Meredith, and D. B. Dingwell (2013), Reconstructing magma failure and the degassing network of dome-building eruptions, *Geology*, *41*(4), 515–518.

Lejeune, A. M., Y. Bottinga, T. W. Trull, and P. Richet (1999), Rheology of bubble-bearing magmas, *Earth Planet. Sci. Lett.*, *166*(1–2), 71–84.

Llewellin, E. W., and M. Manga (2005), Bubble suspension rheology and implications for conduit flow, *J. Volcanol. Geotherm. Res.*, *143*(1–3), 205–217.

Loughlin, S. C., R. Luckett, G. Ryan, T. Christopher, V. Hards, S. De Angelis, L. Jones, and M. H. Strutt (2010), An overview of lava dome evolution, dome collapse and cyclicity at Soufrière Hills Volcano, Montserrat, 2005–2007, *Geophys. Res. Lett.*, *37*, L00E16, doi:10.1029/2010GL042547.

Lovejoy, S., H. Gaonac'h, and D. Schertzer (2004), Bubble distributions and dynamics: The expansion-coalescence equation, *J. Geophys. Res.*, *109*, B11203, doi:10.1029/2003JB002823.
Mader, H. M., E. W. Llewellin, and S. P. Mueller (2013), The rheology of two-phase magmas: A review and analysis, *J. Volcanol. Geotherm. Res.*, *257*, 135–158.
Manga, M., J. M. Castro, K. V. Cashman, and M. Loewenberg (1998), Rheology of bubble-bearing magmas, *J. Volcanol. Geotherm. Res.*, *87*(1–4), 15–28.
Matthews, S. J., M. C. Gardeweg, and R. S. J. Sparks (1997), The 1984 to 1996 cyclic activity of Lascar Volcano, northern Chile: Cycles of dome growth, dome subsidence, degassing and explosive eruptions, *Bull. Volcanol.*, *59*(1), 72–82.
Melnik, O., A. A. Barmin, and R. S. J. Sparks (2005), Dynamics of magma flow inside volcanic conduits with bubble overpressure buildup and gas loss through permeable magma, *J. Volcanol. Geotherm. Res.*, *143*, 53–68.
Mueller, S., O. Melnik, O. Spieler, B. Scheu, and D. B. Dingwell (2005), Permeability and degassing of dome lavas undergoing rapid decompression: An experimental determination, *Bull. Volcanol.*, *67*(6), 526–538.
Mueller, S., B. Scheu, O. Spieler, and D. B. Dingwell (2008), Permeability control on magma fragmentation, *Geology*, *36*(5), 399–402.
Mueller, S., B. Scheu, U. Kueppers, O. Spieler, D. Richard, and D. B. Dingwell (2011), The porosity of pyroclasts as an indicator of volcanic explosivity, *J. Volcanol. Geotherm. Res.*, *203*(3–4), 168–174.
Nairn, I. A., S. Self, J. W. Cole, G. S. Leonard, and C. Scutter (2001), Distribution, stratigraphy and history of proximal deposits from the c. AD 1305 Kaharoa eruption of Tarawera volcano, New Zealand, *N. Z. J. Geol. Geophys.*, *44*(3), 467–484.
Nairn, I. A., P. Shane, J. W. Cole, G. S. Leonard, S. Self, and N. Pearson (2004), Rhyolite magma processes of the ~ AD 1315 Kaharoa eruption episode, Tarawera volcano, New Zealand, *J. Volcanol. Geotherm. Res.*, *131*, 265–294.
Nakada, S., H. Shimizu, and K. Ohta (1999), Overview of the 1990–1995 eruption at Unzen Volcano, *J. Volcanol. Geotherm. Res.*, *89*, 1–22.
Nakamura, M., K. Otaki, and S. Takeuchi (2008), Permeability and pore-connectivity variation of pumices from a single pyroclastic flow eruption: Implications for partial fragmentation, *J. Volcanol. Geotherm. Res.*, *176*(2), 302–314.
Nara, Y., P. G. Meredith, T. Yoneda, and K. Kaneko (2011), Influence of macro-fractures and micro-fractures on permeability and elastic wave velocities in basalt at elevated pressure, *Tectonophysics*, *503*(1–2), 52–59.
Okumura, S., and O. Sasaki (2014), Permeability reduction of fractured rhyolite in volcanic conduits and its control on eruption cyclicity, *Geology*, *42*(10), 843–846.
Okumura, S., M. Nakamura, S. Takeuchi, A. Tsuchiyama, T. Nakano, and K. Uesugi (2009), Magma deformation may induce non-explosive volcanism via degassing through bubble networks, *Earth Planet. Sci. Lett.*, *281*(3–4), 267–274.
Picard, D., L. Arbaret, M. Pichavant, R. Champallier, and P. Launeau (2011), Rheology and microstructure of experimentally deformed plagioclase suspensions, *Geology*, *39*(8), 747–750.
Pistone, M., L. Caricchi, P. Ulmer, L. Burlini, P. Ardia, E. Reusser, F. Marone, and L. Arbaret (2012), Deformation experiments of bubble- and crystal-bearing magmas: Rheological and microstructural analysis, *J. Geophys. Res.*, *117*, B05208, doi:10.1029/2011JB008986.
Proussevitch, A. A., and D. L. Sahagian (1996), Dynamics of coupled diffusive and decompressive bubble growth in magmatic systems, *J. Geophys. Res.*, *101*(B8), 17,447–17,445, doi:10.1029/96JB01342.
Quane, S. L., and J. K. Russell (2005), Welding: Insights from high-temperature analogue experiments, *J. Volcanol. Geotherm. Res.*, *142*(1–2), 67–87.
Quane, S. L., J. K. Russell, and E. A. Friedlander (2009), Time scales of compaction in volcanic systems, *Geology*, *37*(5), 471–474.
Rust, A. C., and K. V. Cashman (2004), Permeability of vesicular silicic magma: Inertial and hysteresis effects, *Earth Planet. Sci. Lett.*, *228*(1–2), 93–107.
Rust, A. C., and M. Manga (2002), Effects of bubble deformation on the viscosity of dilute suspensions, *J. Non-Newtonian Fluid Mech.*, *104*(1), 53–63.
Sahetapy-Engel, S. T., and A. J. L. Harris (2008), Thermal structure and heat loss at the summit crater of an active lava dome, *Bull. Volcanol.*, *71*(1), 15–28.
Schipper, C. I., J. M. Castro, H. Tuffen, M. R. James, and P. How (2013), Shallow vent architecture during hybrid explosive–effusive activity at Cordón Caulle (Chile, 2011–12): Evidence from direct observations and pyroclast textures, *J. Volcanol. Geotherm. Res.*, *262*, 25–37.
Shields, J. K., H. M. Mader, M. Pistone, L. Caricchi, D. Floess, and B. Putlitz (2014), Strain-induced outgassing of three-phase magmas during simple shear, *J. Geophys. Res. Solid Earth*, *119*, 6936–6957, doi:10.1002/2014JB011111.
Smith, J. V., Y. Miyake, and T. Oikawa (2001), Interpretation of porosity in dacite lava domes as ductile—brittle failure textures, *J. Volcanol. Geotherm. Res.*, *112*, 25–35.
Sparks, R. S. J. (1978), The dynamics of bubble formation and growth in magmas: A review and analysis, *J. Volcanol. Geotherm. Res.*, *3*(1–2), 1–37.
Sparks, R. S. J. (1997), Causes and consequences of pressurisation in lava dome eruptions, *Earth Planet. Sci. Lett.*, *150*, 177–189.
Sparks, R. S. J., M. D. Murphy, A. M. Lejeune, R. B. Watts, J. Barclay, and S. R. Young (2000), Control on the emplacement of the andesite lava dome of the Soufriere Hills volcano, Montserrat by degassing-induced crystallization, *Terra Nova*, *12*(1), 14–20.
Spieler, O., B. Kennedy, U. Kueppers, D. B. Dingwell, B. Scheu, and J. Taddeucci (2004), The fragmentation threshold of pyroclastic rocks, *Earth Planet. Sci. Lett.*, *226*(1–2), 139–148.
Takeuchi, S., S. Nakashima, A. Tomiya, and H. Shinohara (2005), Experimental constraints on the low gas permeability of vesicular magma during decompression, *Geophys. Res. Lett.*, *32*, L10312, doi:10.1029/2005GL022491.
Takeuchi, S., S. Nakashima, and A. Tomiya (2008), Permeability measurements of natural and experimental volcanic materials with a simple permeameter: Toward an understanding of magmatic degassing processes, *J. Volcanol. Geotherm. Res.*, *177*, 329–339.
Takeuchi, S., A. Tomiya, and H. Shinohara (2009), Degassing conditions for permeable silicic magmas: Implications from decompression experiments with constant rates, *Earth Planet. Sci. Lett.*, *283*(1–4), 101–110.
Tuffen, H., D. B. Dingwell, and H. Pinkerton (2003), Repeated fracture and healing of silicic magma generate flow banding and earthquakes?, *Geology*, *31*(12), 1089–1092.
Vallance, J. W., D. J. Schneider, and S. P. Schilling (2008), Growth of the 2004–2006 lava-dome complex at Mount St. Helens, Washington, in *A Volcano Rekindled: The Renewed Eruption of Mt St Helens, 2004–2006*, edited by D. R. Sherrod, W. E. Scott, and P. H. Stauffer, *U.S. Geol. Surv. Prof. Pap.*, *1750*, pp. 169–208.
Vasseur, J., F. B. Wadsworth, Y. Lavallée, K.-U. Hess, and D. B. Dingwell (2013), Volcanic sintering: Timescales of viscous densification and strength recovery, *Geophys. Res. Lett.*, *40*, 5658–5664, doi:10.1002/2013GL058105.
von Aulock, F. W. (2013), Bubbles, crystals and cracks in cooling magma, PhD thesis, Dep. of Geol. Sc., Univ. of Canterbury, Christchurch, New Zealand.
von Aulock, F. W., A. R. L. Nichols, B. M. Kennedy, and C. Oze (2013), Timescales of texture development in a cooling lava dome, *Geochim. Cosmochim. Acta*, *114*, 72–80.
Wadge, G., G. Ryan, and E. S. Calder (2009), Clastic and core lava components of a silicic lava dome, *Geology*, *37*(6), 551–554.
Wadsworth, F. B., J. Vasseur, F. W. von Aulock, K.-U. Hess, B. Scheu, Y. Lavallée, and D. B. Dingwell (2014), Nonisothermal viscous sintering of volcanic ash, *J. Geophys. Res. Solid Earth*, *119*, 8792–8804, doi:10.1002/2014JB011453.
Watts, R. B., R. A. Herd, R. S. J. Sparks, and S. R. Young (2002), Growth patterns and emplacement of the andesitic lava dome at Soufriere Hills Volcano, Montserrat, *Geol. Soc. London Mem.*, *21*(1), 115–152.

Webb, S. L., and D. B. Dingwell (1990), Non-Newtonian rheology of igneous melts at high stresses and strain rates: Experimental results for rhyolite, andesite, basalt and nephelinite, *J. Geophys. Res.*, *95*, 15,695–15,701.

Wright, H. M. N., and R. F. Weinberg (2009), Strain localization in vesicular magma: Implications for rheology and fragmentation, *Geology*, *37*(11), 1023–1026.

Wright, H. M. N., K. V. Cashman, E. H. Gottesfeld, and J. J. Roberts (2009), Pore structure of volcanic clasts: Measurements of permeability and electrical conductivity, *Earth Planet. Sci. Lett.*, *280*(1–4), 93–104.

Yokoyama, T., and S. Takeuchi (2009), Porosimetry of vesicular volcanic products by a water-expulsion method and the relationship of pore characteristics to permeability, *J. Geophys. Res.*, *114*, B02201, doi:10.1029/2008JB005758.

Yoshimura, S., and M. Nakamura (2008), Diffusive dehydration and bubble resorption during open-system degassing of rhyolitic melts, *J. Volcanol. Geotherm. Res.*, *178*(1), 72–80.